IOP Publishing Measurement Science and Technology
Meas. Sci. Technol. **31** (2020) 055902 (14pp) https://doi.org/10.1088/1361-6501/ab6521

A dynamic hysteresis meter for studying ferrofluids designed for magnetic hyperthermia

A H Sámano[1], S Rosales[2], E E Mazon[1], N Casillas[2], A Topete[3], J A Paz[1], L H Quintero[1], J C Estrada[1] and M E Cano[1,4]

[1] Centro Universitario de la Ciénega, Universidad de Guadalajara. Av. Universidad 1115, col. Linda Vista, CP 47820, Ocotlán, Jalisco, Mexico
[2] Centro Universitario de Ciencias Exactas e Ingenierías, Blvd. Marcelino García Barragán 1421, col. La Loma, CP 44430, Guadalajara, Jalisco, Mexico
[3] Centro Universitario de Ciencias de la Salud, Sierra Mojada 950, col. Independencia, CP 44340, Guadalajara, Jalisco, Mexico

E-mail: eduardo.cano@cuci.udg.mx and meduardo2001@hotmail.com

Received 4 September 2019, revised 10 December 2019
Accepted for publication 23 December 2019
Published 26 February 2020

Abstract

An AC magnetometer system is developed to determine the specific absorption rate (SAR) of ferrofluids designed to work in the range of interest for magnetic hyperthermia. The experimental setup contains a set of configurable *RL* coil sensors (resistance plus inductance) to obtain the inner area of the dynamic hysteresis loops of colloidal dispersions, which are stimulated using a multi-range alternating magnetic field generator. This magnetometer is suitable for covering the frequency band of 100–450 kHz, and special considerations concerning sample size and placement inside the magnetic field region are taken into account. The performance of the system is tested using a ferrofluid of water-dispersed iron oxide nanoparticles. The SAR determined with the developed system is compared with that obtained using the typical calorimetric procedure. The observations are consistent with both kinds of measurement, and also coincide with the results for other previously reported experimental systems.

Keywords: hyperthermia, resonant inverter, SAR, ferrofluid, magnetization

1. Introduction

Currently, the synthesis of new magnetic nanoparticle (MNP) ferrofluids for biomedical applications is being widely studied. For example, for magnetic hyperthermia therapy a quite stable colloidal dispersion of MNPs is stimulated with high-frequency magnetic fields of amplitude H and frequency f. Typically, the desired ferrofluid (with density ρ) for use in cancer therapy has a high power absorption density P. This parameter can be characterized by its specific absorption rate (SAR) in units of W g^{-1} and both quantities are related through the constant of proportionality ρ. Thus, significant heating of cells or tissues could be expected to require a minimal ferrofluid dose.

The magnitude of P can be directly estimated using calorimetric experiments. Another direct way is through dynamic hysteresis loop (DHL) measurements. In this respect, few works covering the frequency range above 100 kHz (the magnetic hyperthermia range) have been published. For example, a system to obtain SAR via calorimetric and DHL procedures was built by Bekovic and Hamler [1]. In this study, a high-frequency range wass swept using magnetic field amplitudes of a few mT. A similar experimental setup was used by Nakamura *et al* [2]. Later, with the device developed by Connord *et al* [3], the reproducibility of DHL measurements was analyzed at 80 mT, with many complications for frequencies above 56 kHz. In a recent paper, Guibert *et al* [4] realized

[4] Author to whom any correspondence should be addressed.

DHL measurements over an interval of 111 kHz at 15 mT and 628 kHz at 4.3 mT.

On the other hand, considering the experimental work of Connord *et al*, it is remarkable how the reproducibility of the DHL depends on several factors, such as the dimension of the samples, the placement of the ferrofluid inside the magnetic field and the impedance response of the pickup coil sensor. As can be expected, the signal/noise (s/n) ratio of these sensors diminishes with increase in frequency. In this sense, a phase-shift θ between the induced voltage and the applied field amplitude H must be taken into account for high frequencies. In this respect, extensive experimental work has been performed by Garaio *et al* [5–7], who used a magnetic field generator complemented with an AC magnetometer ranging from 149 kHz at 37 kA m^{-1} up to 1030 kHz at 22 kA m^{-1}. In that work, a complex function $g(f)$ was introduced to mathematically compensate for the intrinsic variations of $|Z|$ and θ in the estimated magnetization through the pickup coils.

In previous work, Mazón *et al* [8] developed a magnetic field generator with high-frequency resolution [9] which was connected with a resonant frequency tracker system [9]. The device can work in the interval 180–532 kHz, with an amplitude of up to 35 mT. Indeed, in this new research the magnetic field generator is slightly modified and complemented with an AC magnetometer composed of three configurable *RL* (resistance plus inductance) circuits designed to measure the SAR of ferrofluids. The experimental work is particularly careful about sample size and its placing in the magnetic field and includes linear compensation for θ. These important considerations (which have been omitted in several cited papers) increase the reproducibility of the DHL measurements.

2. Theoretical background

2.1. Modeling the heating capability of ferrofluids

The relationship between the previously mentioned physical parameters P and SAR [10] is mathematically described in equation (1). In the laboratory the SAR is usually determined using a fluoroptic temperature probe placed inside the ferrofluid (with specific heat C_p), which is warmed due to the alternating induced magnetization. Then, the rise in temperature is measured along time and the SAR is estimated using equation (2) [11] (previously the weight factor m_t/m_{np} was introduced, where m_t and m_{np} are the mass of the ferrofluid and MNPs, respectively [12, 13]):

$$P = \rho \times \mathrm{SAR} \tag{1}$$

$$\mathrm{SAR} = C_p \frac{\mathrm{d}T}{\mathrm{d}t} \frac{m_t}{m_{np}}. \tag{2}$$

In general, when a distribution of MNPs presents an effective superparamagnetic behavior, the magnitude of P obeys equation (3)[14], which intrinsically includes the magnetic Néel–Brown relaxation time τ_N and the Brownian relaxation time τ_B, both of which are included in the effective relaxation time τ. Also considered in equation (3) are its magnetic susceptibility χ_F and the permeability of the empty space μ_0. Then, several complications can be expected in the determination of P if the diameter of the MNPs is not uniform; τ depends exponentially on the particle volumes V and their magnetic anisotropy constants κ (the Arrhenius law). Also, a linear dependence of V is implicit in τ_B.

Another way to determine P by obtaining (via magnetization measurements) the DHL of the ferrofluid is presented by equation (4) [15]; indeed, this alternative does not depend explicitly on τ:

$$P = \pi \mu_0 \chi_\mathrm{F} H^2 f \left(\frac{2\pi f \tau}{1 + (2\pi f \tau)^2} \right) \tag{3}$$

$$P = \mu_0 f \oint \vec{M} \cdot \mathrm{d}\vec{H}. \tag{4}$$

2.2. Modeling the AC magnetometer system

The use of inductive sensors to probe alternating magnetic fields is based on the Faraday and Lenz laws, where the induced voltage V_emf is expressed in equation (5):

$$V_\mathrm{emf} = -n \cdot \frac{\mathrm{d}\Phi}{\mathrm{d}t} = -S_\mathrm{coil} \cdot n \cdot \frac{\mathrm{d}B}{\mathrm{d}t}. \tag{5}$$

In this equation, n is the number of turns of the coil sensor, $\Phi = \vec{B} \cdot \mathrm{d}\vec{s}$ is the magnetic flux passing through the coil cross-section surface S_coil and B is the magnitude of the magnetic field. Typically, the frequency response of the coil sensors is not limited, thus the acquired signals have a superposed high amount of noise. The most common way to discard the unwanted noise signals is to use an array of two identical sensor coils working differentially; these are placed at two separated spatial points and only one of them detects the noise. The first-order gradiometer coil sensor is an efficient differential array which has the capability to detect magnetic flux including spatial derivative components [16]. Axial gradiometers, like that displayed in figure 1(a), are composed of two identical coils (L_u and L_d) wound in the opposite sense and connected in series. Also, their dimensions satisfy the constriction [17] given in equation (6), where h is the coil separation and r the coil radius:

$$h = \sqrt{3} \cdot r. \tag{6}$$

Considering equation (5) for a gradiometer device, the induced voltage V_emf due to a volumetric magnetized sample is given by equation (7), which can be reduced as equation (8):

$$v_\mathrm{emf} = -\mu_0 n S_m \cdot \frac{\mathrm{d}[(M+H) - (kM+H)]}{\mathrm{d}t} \tag{7}$$

$$= -\mu n S_m \cdot \frac{\mathrm{d}\,[M\,(1+k)]}{\mathrm{d}t} = -\mu_0 n S_m\,(1+k)\,\frac{\mathrm{d}\,[M]}{\mathrm{d}t}. \tag{8}$$

Here S_m is the cross section of the sample and k is a compensation factor. According to equation (8), the magnetization of the samples can be estimated by integrating the gradiometer signals. For idealized point magnetic sources, the parameter k vanishes and the lower coil of the gradiometer L_d only reads the external noise. Otherwise, the parameter k depends on

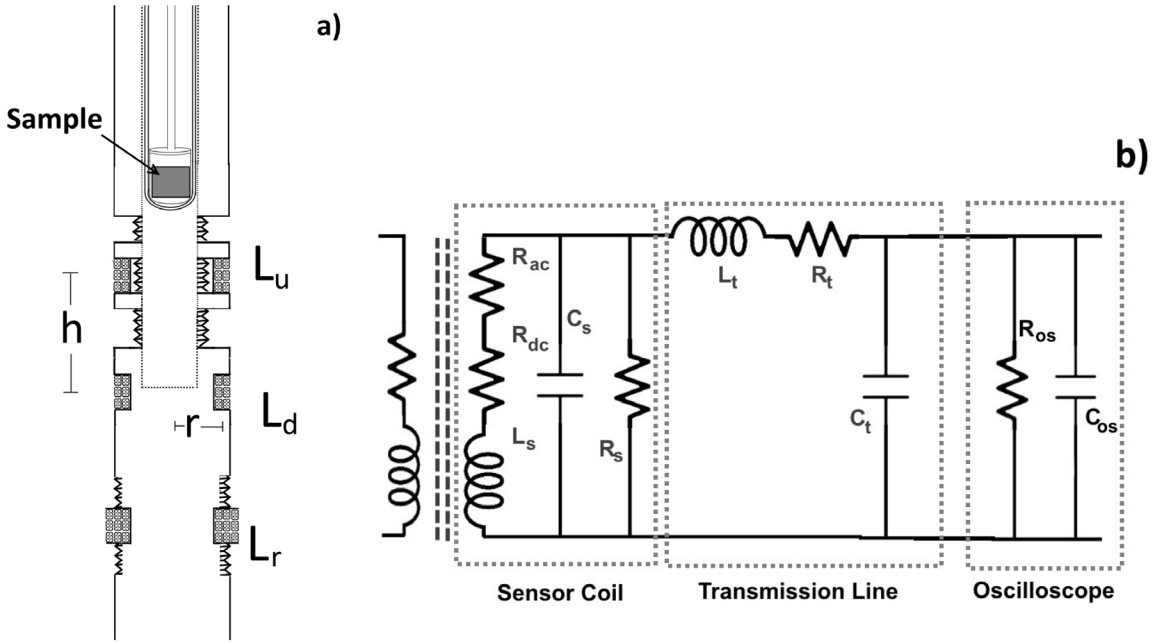

Figure 1. (a) First-order axial gradiometer comprising coils L_u plus L_d including a third coil L_r. (b) Schematic diagram of the equivalent circuit connection between the gradiometer and the oscilloscope, through a transmission line.

sample magnetization M, its size and the relative position of the sample inside the gradiometer plus sample density or concentration [18]. Several works [1–5] have ignored this parameter and assumed an ideal behavior of the magnetized samples. This ideal assumption could be a reasonable approximation for small solid samples and for highly diluted ferrofluids. An alternative way to determine the parameter k is to include a third induction coil L_r away from the gradiometer coils (see figure 1(a)) which can be used as a reference sensor to separately determine the differential amplitude induced between L_u and L_r (ΔV_{u-r}) and similarly between L_d and L_r (ΔV_{d-r}). Then, the compensation factor is given by equation (9). Thus, when a point sample is magnetized the numerator $\Delta V_{d-r} = 0$ is obtained and $k \to 0$, as expected:

$$k = \frac{\Delta V_{d-r}}{\Delta V_{u-r}}. \tag{9}$$

On the other hand, the gradiometer can be modeled as the *RLC* circuit displayed in figure 1(b), where the electronic parameters L_s, $R_{\rm dc}$ and $R_{\rm ac}$ are the inductance, DC Ohmic resistance and AC impedance due to the skin effect, respectively. Also, C_s is the internal capacitance associated with the coil loops and R_s is a parallel loading resistance, which is used to create a linear response in the impedance curve along with a set of frequencies.

The transmission line also depicted in figure 1(b) represents the equivalent circuit of the cable connecting the sensor coil to the acquisition device with characteristic series impedance $Z_{tl} = \sqrt{R_t + {\rm i}\omega L_t / G_t + {\rm i}\omega C_t}$, where ω is the angular frequency, R_t and L_t the series resistance and inductance of the cable and G_t and C_t are the conductance and capacitance between the two conductors forming the cable.

According to Ueda and Watanabe [19], Z_{t0} can be ignored when the frequency of the higher significant harmonic of the signal obeys the inequality $\omega C_t R_t \ll 1$ and at the same time the input impedance of the acquisition device (such as a digital oscilloscope) must be larger than R_t. In which case, the voltage amplitude at the acquisition end of the cable is expressed by equation (10):

$$V_{\rm adq} = V_{\rm sc} \frac{1}{1 + R_t / Z_{\rm ad}}. \tag{10}$$

On the other hand, the impedance of the sensor coil can be fitted to the equivalent impedance given by equation (11):

$$Z_{\rm eq} = \frac{1}{Y}, \tag{11}$$

where the equivalent admittance is $Y_s = \frac{1}{Z_1} + \frac{1}{Z_2} + \frac{1}{R_s}$, which contains the impedances $Z_1 = R_L + {\rm i}2\pi f L_s$ and $Z_2 = -\frac{\rm i}{2\pi f C_s}$. The resistance R_L is the total resistive loss of the sensor coil, so we have $R_L = R_{\rm dc} + R_{\rm ac}$. In Figure 2(a), an illustration of $|Z_{\rm eq}|$ and its phase θ (with normalized units) is shown. In the first plot of $|Z_{\rm eq}|$ (dark continuous line), $R_s \to Op$ (open circuit) is considered, whereas $R_s = 100\ \Omega$ is assumed in the dark dashed line plot. In this same sense, the full and open symbols correspond to θ, with $R_s \to Op$ and $R_s = 100\ \Omega$, respectively. All these dependences are plotted along the normalized frequencies, taking the typical values $L_s = 3\ \mu$H, $R_L = 3\ \Omega$ and $C_s = 50$ pF.

As a consequence of R_s, the initial magnitude $|Z_{\rm eq}|$ suffers dramatic modifications in its waveform, replacing the characteristic peak of a resonant value ($R_s \to Op$) in f_0 for an almost constant behavior ($R_s = 100\ \Omega$). Similarly, the phase θ is not maintained constant along f because it initially increases to reach a maximum value and then slowly decreases. All these drastic differences can be explained by analyzing the Q factor under the same two situations of R_s. Initially, the resonant frequency f_0 depends only on the reactive branches of the circuit.

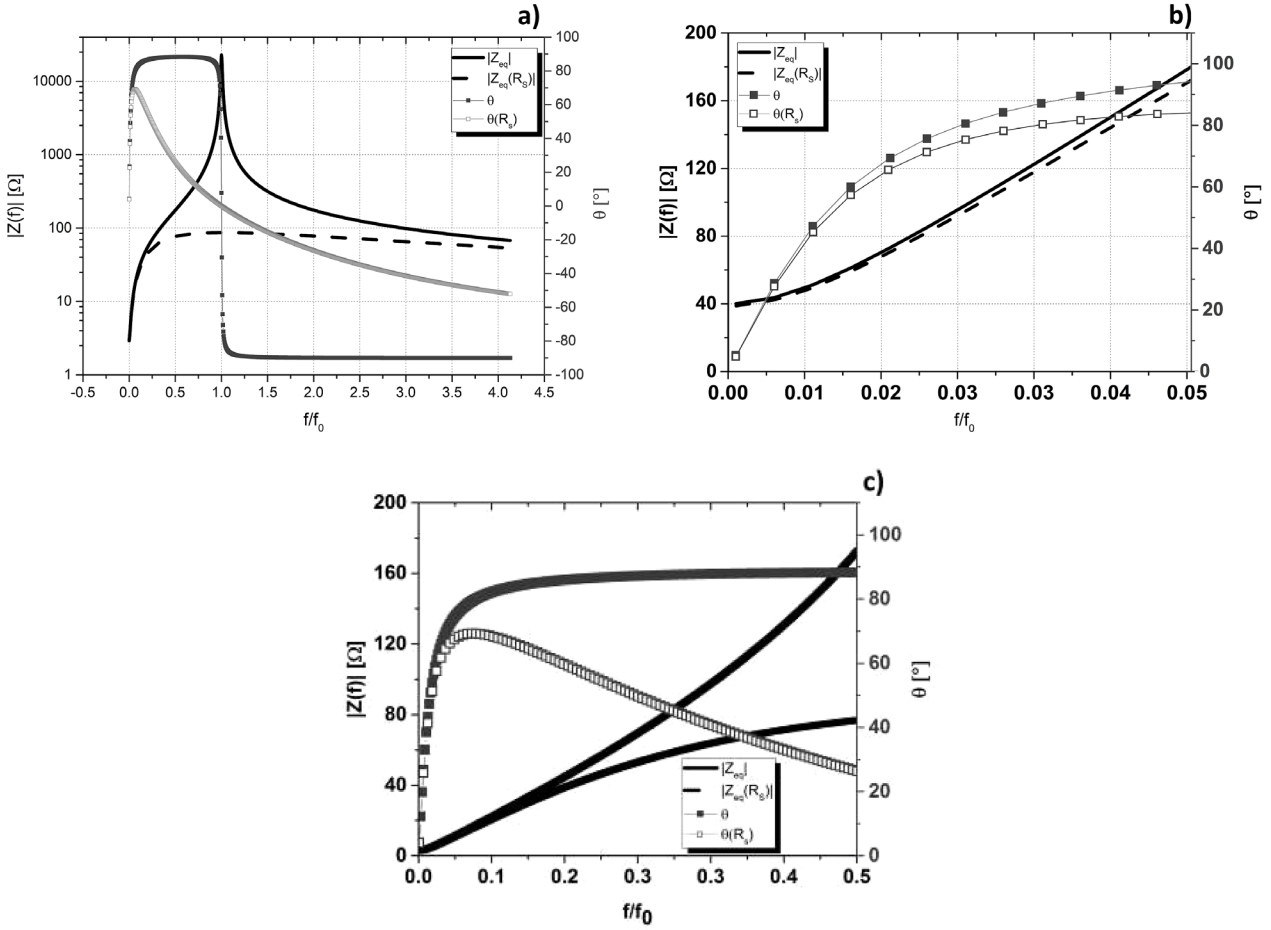

Figure 2. (a) Plots of $|Z_{eq}|$ and θ (in normalized units) with $R \rightarrow Op$ (dark continuous line and full symbols, respectively) and $R = 100\ \Omega$ (dark dashed line and open symbols, respectively). (b) A close-up of $|Z_{eq}|$ and θ over the normalized frequency interval $0 < f/f_0 < 0.05$. (c) Another close-up of of $|Z_{eq}|$ and θ over the normalized frequency interval $0 < f/f_0 < 0.5$.

This is described in equation (12) and leads to the Q factor [19] given by equation (13). Thus, Q is clearly different from the Q_{Rs} factor reached by considering R_s as is expressed in equation (14). Hence, the inequality relation $Q_{Rs} < Q$, can be generally expected:

$$f_0 = \frac{1}{2\pi}\sqrt{\frac{1}{C_s L_s} - \frac{R_L^2}{L_s^2}} \approx \frac{1}{2\pi\sqrt{C_s L_s}} \tag{12}$$

$$Q = \frac{1}{R_L}\sqrt{\frac{L_s}{C_s}} \tag{13}$$

$$Q_{R_s} = \frac{R_s\sqrt{L_s C_s}}{L_s + C_s R_s R_L} = Q\left(\frac{C_s R_s R_L}{L_s + C_s R_s R_L}\right). \tag{14}$$

Following the discussion on R_s, figure 2(b) shows a close-up view of $|Z_{eq}|$ and θ along the normalized interval $0 < f/f_0 < 0.05$. In this zoom of all the plots of figure 2(a), differences of less than 10% in both parameters $|Z_{eq}|$ and θ are determined when $R_s = 100\ \Omega$. This observation indicates an almost negligible effect of R_s on the fundamental frequencies of the sensed signal through the gradiometer. In the same sense, an interval 10 times higher is now observed in the close-up view displayed in figure 2(c). A clear diminution of $|Z_{eq}|$ is evidenced when $R_s = 100\ \Omega$. Thus a typical response resembling a low-pass filter of the gradiometer sensor is observed. Indeed, this is a better response than the band rejection-like behavior presented when $R_s \rightarrow Op$, where the fast increase in $|Z_{eq}|$, implies a high rejection of frequencies of the first 10 harmonics of the signal registered by the sensor coil. Nevertheless, the almost linear diminution of θ along f/f_0 (when $R_s = 100\ \Omega$) represents a clear disadvantage which must be mathematically compensated.

3. Materials and methods

3.1. Description of the experimental setup

Regarding the sensing system described in figures 1(a) and (b), in this new experimental setup $L_s = 3.21\ \mu$H, $R_L = 4.37\ \Omega$ and $C_s = 14.9$ pF are the determined electric parameters of our gradiometer system, which are measured with a Hioki RLC meter IM3536. Additionally, $R_s = 84.4\ \Omega$ is the experimentally chosen loading resistance. Furthermore, the gradiometer characteristics are six turns per coil of 46 AWG Litz wire (10 strands), also $d_s = 14$ mm and $h = 12$ mm are the diameter and minimum separation between L_u and L_d, respectively. Additionally, the reference coil has inductance

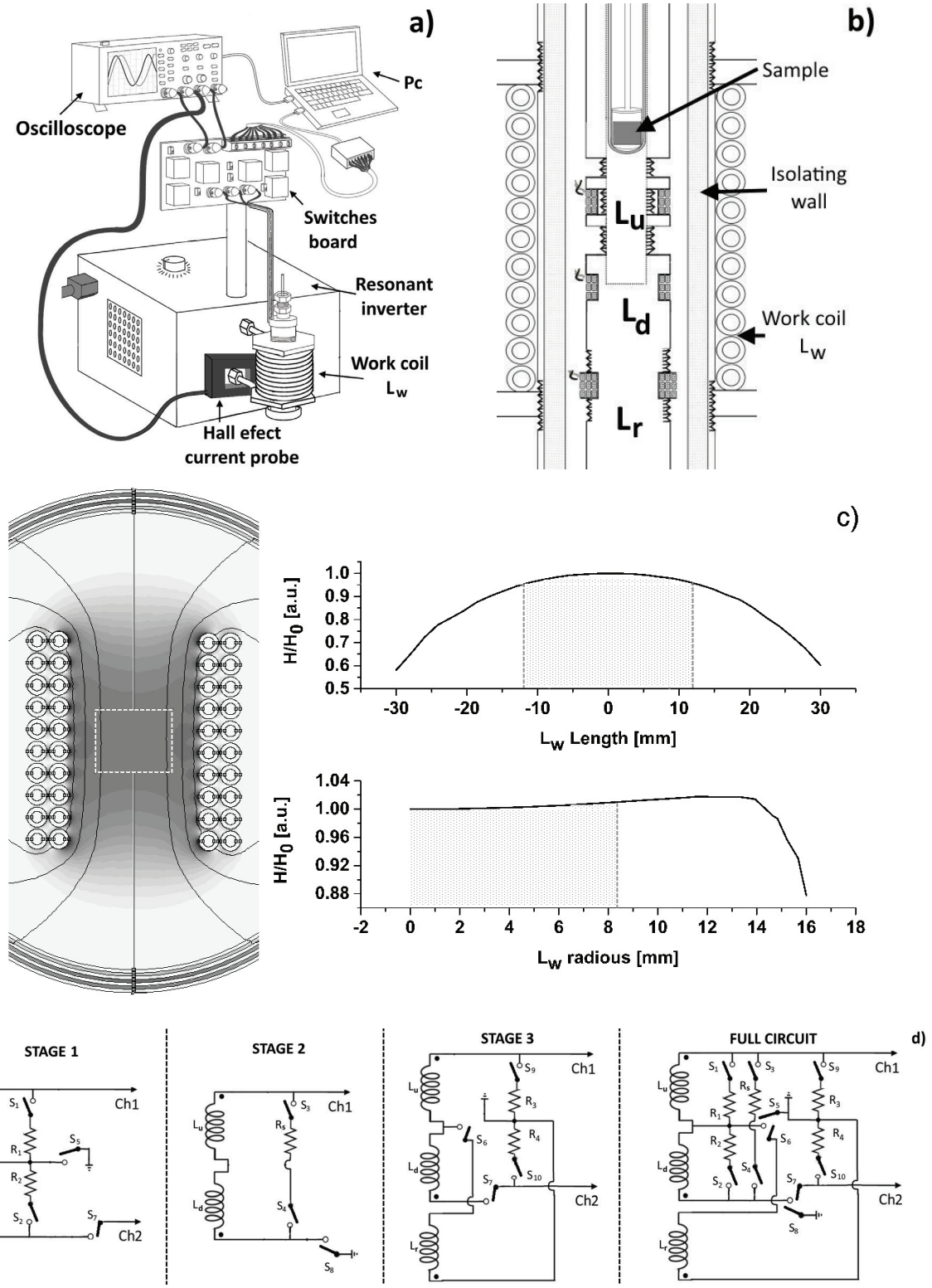

Figure 3. (a) The whole experimental setup. (b) A close-up transverse view of the hysteresis meter, placed inside the magnetic field generator coil. (c) The computed magnetic field distribution around the coil and a plot of its axial and radial normalized dependences. (d) The full circuit diagram of the *RL* sensors and the three individual electronic stages.

$L_r = 2.7\ \mu$H and resistance $R_{rdc} = 3.27\ \Omega$. It is constructed with $N = 10$ Litz wires, reaching a transverse diameter $d_r = 14$ mm and length $l_r = 4$ mm. All the coils are wound around cylindrical PVC pipes in such a way that the separation between L_d and L_r and between L_d and L_u can be finely adjusted; this is schematized in figure 1(a). The main idea of this coil configuration is to reach an optimum separation h, which guarantees the correct annulment of the applied magnetic field H. At the same time, L_r is used to indicate if the sample size or its placing inside the magnetic field region influences solely

the upper gradiometer coil. These considerations are important for removing uncertainty in the measurement of induced electromotive forces.

The whole experimental setup is schematized in figure 3(a); it is important to highlight that the magnetic field generator used is well described by Mazón *et al* [8, 9]. In those works, a variable amplitude and frequency system to determine the SAR and P of ferrofluids was constructed and tested, using the typical magneto-calorimetric procedure. For the purposes of this study, the exposed induction coil L_w was modified, reaching $N_w = 20$ wires, with a height and diameter of $h_w = 60$ mm and $d_w = 32$ mm, respectively, and covering the frequency range 100–450 kHz and up to 30 mT amplitude. The AC hysteresis meter was placed and fastened inside the empty space of L_w and its voltage measured through an oscilloscope (Rigol DS1052E). Furthermore, a 2 MHz high-current Hall sensor (Tektronix TCP404XL) was complemented with an amplifier system (TCPA400) to measure the current I circulating through L_w. Accordingly, the applied H on the samples is estimated using the typical solenoid equation given in equation (15):

$$H = IN_w h_w^{-1}. \tag{15}$$

Additionally, in a further step, a fluoroptic thermometer (Luxtron One) was used to sense the sample temperature and was connected to a computer using an interface in the LabView environment. Figure 3(b) shows a close-up of a transverse view of the coil system. In this scheme, the sample is placed in a cylindrical chamber which is vertically displaced inside the empty space towards the center of the upper gradiometer coil L_u. Likewise, there is an isolating wall between the copper pipe wires of L_w and the walls of all parts of the sensing coil system. In addition, a water chiller apparatus is connected to L_w to maintaining it at room temperature.

In order to have an idea of the shape of the magnetic field, the distribution of flux lines is schematized by a finite element calculation using Femm 4.2 software, taking the parameters of L_w shown in figure 3(c). The dashed line depicts a region with an area of 20 mm × 16.5 mm, where the homogeneity of H is approximately 95% along the z-axis and 98% for the r-axis. Thus, this area represents a restriction on the sample size that can be analyzed with this experimental setup. Furthermore, this area is used to complement the design and placing of the gradiometer device inside L_w.

In the same sense, in figure 3(d) a circuit diagram with the sensing system of figure 1(a) is shown. As can be seen, it includes L_d, L_r and L_u, which can be connected with a set of resistances through a number of switches following the procedure summarized in three stages (see table 1) and explained below.

Once the magnetic field has been generated, establishing f and H, the next stages are followed to carry out the calibration and measurements with this experimental setup:

- Stage 1: the series resistances $R_1 = R_2 = 1$ MΩ are enabled through the switch configuration described in the second row of Table 1. Then, the resultant induced voltages ΔV_{R1Lu} and ΔV_{R2Ld} are measured, while the coils are axially displaced inside L_w until both voltages reach almost equal values within the homogeneous field region.
- Stage 2: the switches are programmed as in the third row of table 1 and the resistance $R_s = 84.4\ \Omega$ is enabled. So, in absence of a sample, the separation h between L_u and L_d is finely adjusted, reaching an almost null signal produced by the resultant series connection $L_u - L_d$.
- Stage 3, similarly the resistances $R_3 = R_4 = 100\ \Omega$ are enabled (last row of table 1) forming two differential RL arrangements (a resistance in parallel with two series inductances) $R_3||L_u - L_r$ and $R_4||L_d - L_r$, using the reference coil L_r. Afterwards, the ferrofluid is placed and covered inside its cylindrical chamber to be transported up to the central position of the upper coil of the gradiometer. Then the induced voltages ΔV_{u-r} and ΔV_{d-r} at the terminals of $R_3||L_u - L_r$ and $R_4||L_d - L_r$ respectively, allow us to determine the maximum sample size and the compensation factor k of equation (10).
- Finally, once the above three stages have been consecutively completed the device is properly calibrated. Then, Stage 2 is configured again to assess the sample magnetization and to build the DHL.

Table 1. The switch configurations corresponding to each stage, where 0 and 1 mean open and closed states, respectively.

	S1	S2	S3	S4	S5	S6	S7	S8	S9	S10
Stage 1	1	1	0	0	1	0	1	0	0	0
Stage 2	0	0	1	1	0	0	0	1	0	0
Stage 3	0	0	0	0	0	1	1	0	1	1

3.2. Description of the samples

The full experimental setup was tested using three identical samples with 0.5 ml of the same ferrofluid, labeled as FF1, FF2 and FF3. The compound used was a stable colloidal water suspension of magnetite nanoparticles coated with folic acid, at a concentration of 15 mg ml^{-1}. This ferrofluid was prepared in our lab following the well-known co-precipitation method [20].

Initially, a set of four samples were prepared by dispersing 7.5 mg of a drained mass of ferrofluid on 100, 250, 500 and 750 μl of water, labeled as FF-v1, FF-v2, FF-v3 and FF-v4 respectively. This ferrofluid was chosen due to its observed high stability, which is important due to uncertainty caused by sedimentation. These samples were used to analyze the dependence of M on sample volume and to determine the compensation factor k.

Additionally, polydispersed MNPs of silica-coated iron oxide were also synthesized and dried and compressed to form flat disk samples of diameter 12 mm. The disks had masses of 20, 30, 40, 50 and 60 mg and were assigned the respective labels FD-m1, FD-m2, FD-m3, FD-m4 and FD-m5. The coating helps prevent structural change in the iron oxide during sample preparation and analysis. It is important to highlight the estimation of P through equation (4), where the ideal mono-dispersity required in equation (3) is not necessary; in

Table 2. Magnetic properties of the synthesized nanomaterials (dried).

Core	Surface	Core diameter (nm)	Principal magnetic ordering	Magnetic remanence (emu g^{-1})	Magnetic saturation (emu g^{-1})	Blocking temperature (K)	Coercive field (Oe)
Magnetite	Silica	20	Superparamagnetic	0.22	7.0	235	12.5
Magnetite	Folate	13	Superparamagnetic	0.25	49.8	299	1.3

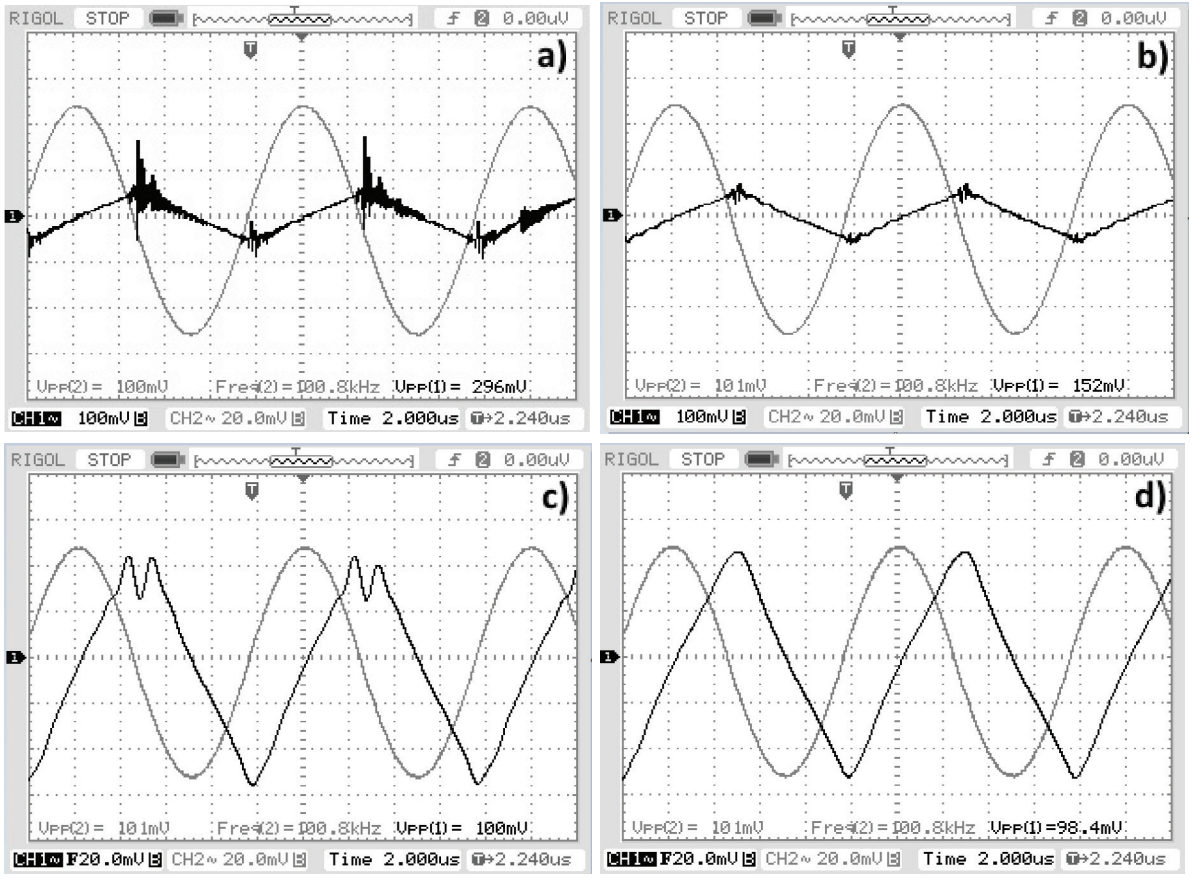

Figure 4. Typical oscilloscope captures of L_w current (CH2) fixing $f = 100.8$ kHz and the induced voltage on the gradiometer terminals (CH1) (a) without a load resistor R_s (open circuit *Op*), (b) with a load resistor $R_s = 84.4\ \Omega$, (c) with $R_s = Op$ plus a digital filter and (d) with $R_s = 84.4\ \Omega$ plus a digital filter.

fact, a linear dependence of M versus H is not needed either. The magnetic properties of both synthesized nanomaterials were measured with a PPMS Versalab and are summarized in table 2. The materials were previously dried at room temperature and the DC magnetization was measured over the interval ± 30 kOe. Also zero-field cooled/field cooled measurements were conducted by sweeping the range $50\,\mathrm{K} < T < 400\,\mathrm{K}$ with 100 Oe of fixed amplitude. Due to polydispersity, they have a principally superparamagnetic ordering, but the registered coercive field indicates the presence of magnetic multidomains producing dipolar interactions.

3.3. Signal processing

With the aim of exemplifying the signal processing of the experimental recordings and highlighting the impact of R_s on the Q_{Rs} factor of the sensors, an initial experiment was conducted using FF1. Then, a set of measurements was obtained with the oscilloscope and recorded in flash memory via USB. For this purpose values of $H = 15$ kA m^{-1} and $f = 100.8$ kHz were set, whereas the switches were configured according to measurement Stage 2 and the resistance R_s was replaced by an open circuit keeping L_u and L_d with resistance $R_L = 4.37\ \Omega$. Figure 4(a) shows the sinusoidal signal of the current crossing L_w (related to H) and the induced voltage in the gradiometer (related to M). This is clearly a noisy signal of M, due to the high-frequency components from the commutation transition of the power inverter circuit that overlap with the environmental signals. Then, the open circuit was replaced by $R_s = 84.4\ \Omega$, which is connected with L_u and L_d, and the same measurements relating to H and M are displayed in figure 4(b). There, the high-frequency noise is significantly attenuated according to the Q_{Rs} factor of equation (14). Moreover, measurements in both figures 4(a) and (b) are digitally low-pass filtered with the Math tools of the oscilloscope, taking up to 10 harmonics of the principal frequency as the cut-off frequency.

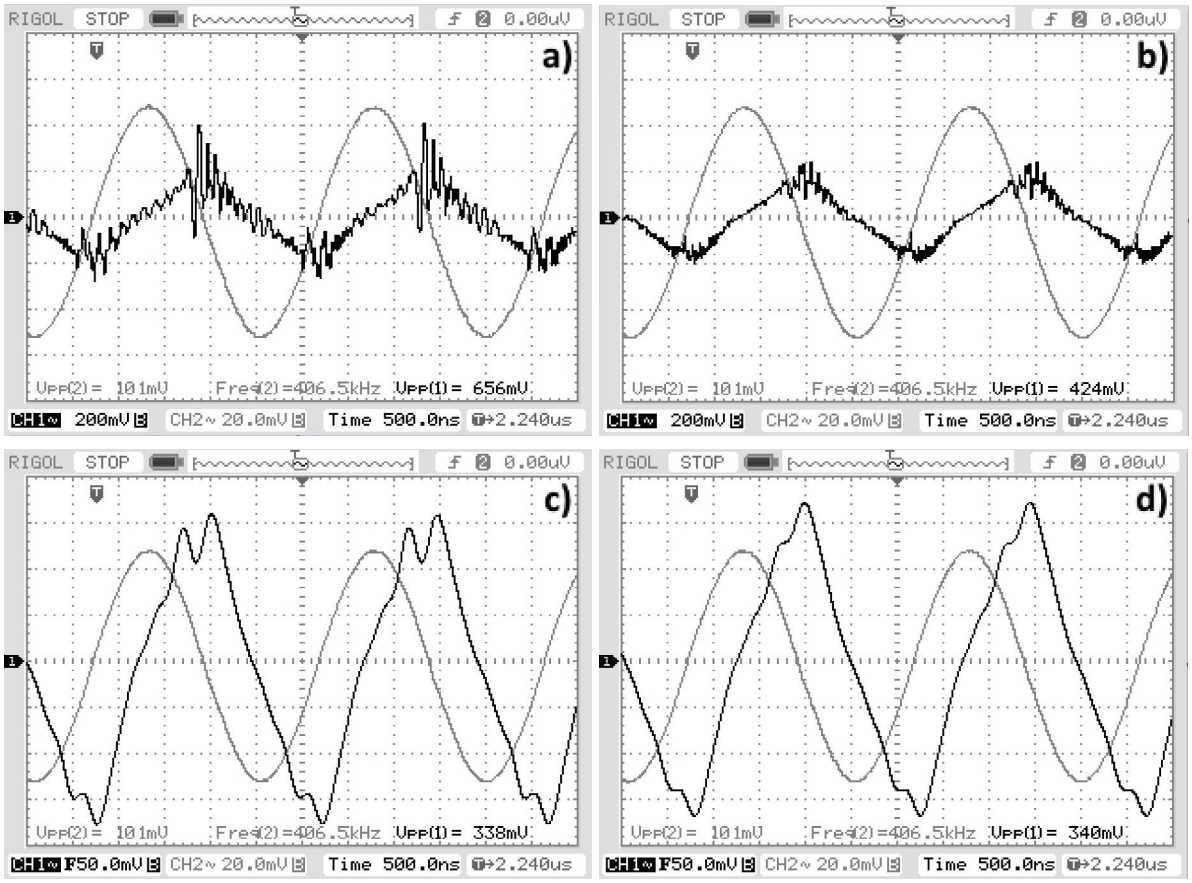

Figure 5. Typical oscilloscope captures of L_w current (CH2) fixing $f = 406.5$ kHz and the induced voltage on the gradiometer terminals (CH1) (a) without a load resistor $R_s = Op$, (b) with a load resistor $R_s = 84.4\ \Omega$, (c) with $R_s = Op$ plus a digital filter and (d) with $R_s = 84.4\ \Omega$ plus a digital filter.

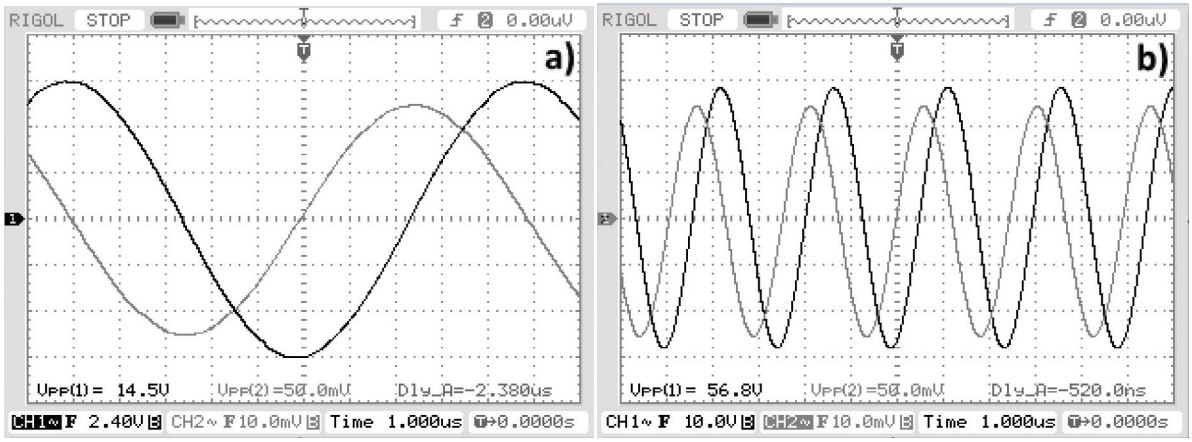

Figure 6. Waveforms of the current I crossing L_w and the induced voltage V on L_u at (a) 100 kHz and (b) 400 kHz. The absolute phase-shifts between I and V are 2.38 μs and 0.52 μs, respectively.

The corresponding filtered signals are shown in figures 4(c) and (d). Through a fast analysis of these last measurements a negligible noise is observed, due to sensitivity to the first harmonics of the signal. However, the inclusion of R_s properly compensates the response of the sensor. The same sequence of measurements was obtained, and is displayed in figures 5(a) and (b), using $f = 406.5$ kHz; the same systematic behavior evidenced in figures 4(a)–(d) is observed. Nevertheless, in this test the suppression of noise was less effective since the cutting frequency is close to the noise frequencies. This noise will not be a problem later on because the posterior digital integration procedure of the voltage waveforms aids in noise suppression.

Regarding the digital low-pass filter f_c of the gradiometer measurements, we have performed several tests (data not shown) considering f_c above the 10th harmonic, but no significant increase in the s/n ratio was observed. Nevertheless, when f_c is reduced a clear trend to a sinusoidal signal shape is

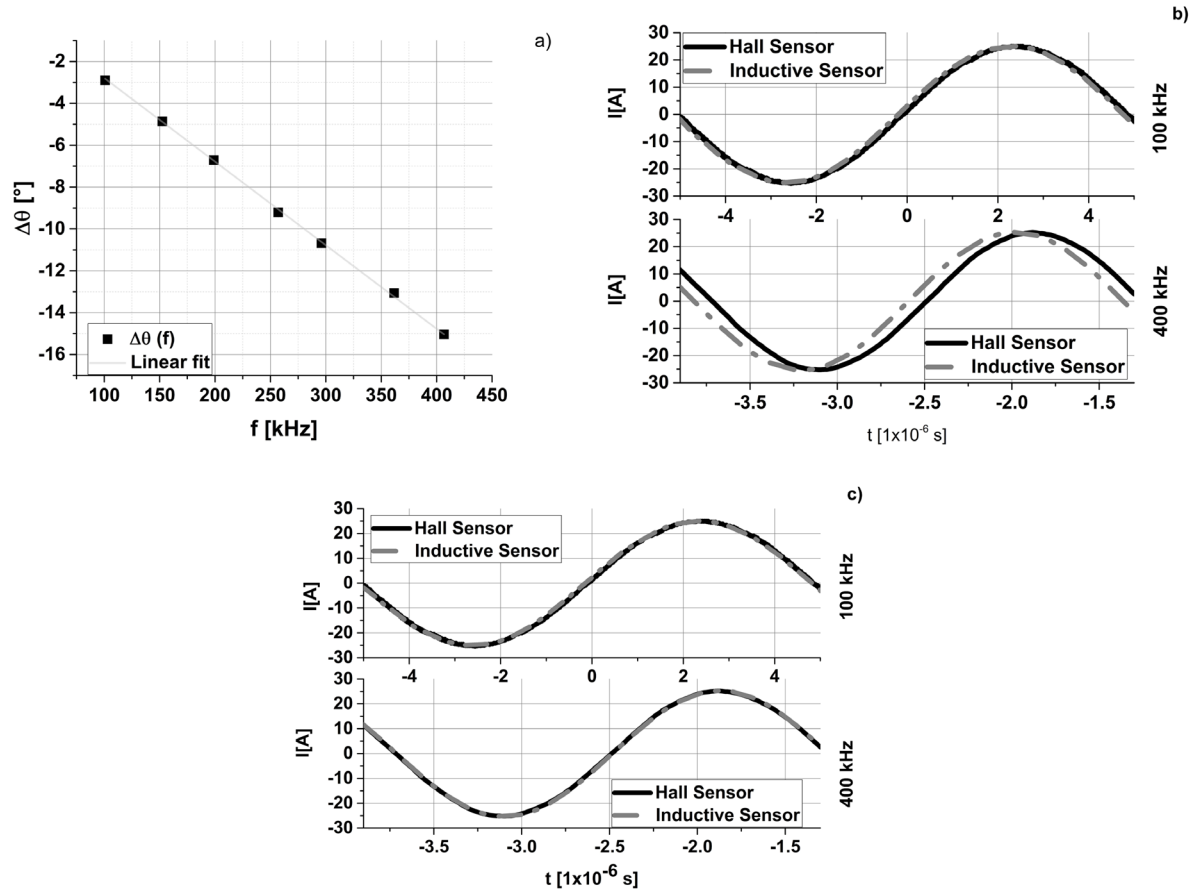

Figure 7. (a) Measured dependence of $\Delta\theta$ versus f using several frequencies of I with the respective linear fit data. (b) The phase-shifted waveforms of I and V at 100 kHz and 400 kHz. (c) The corresponding phase-compensated waveforms.

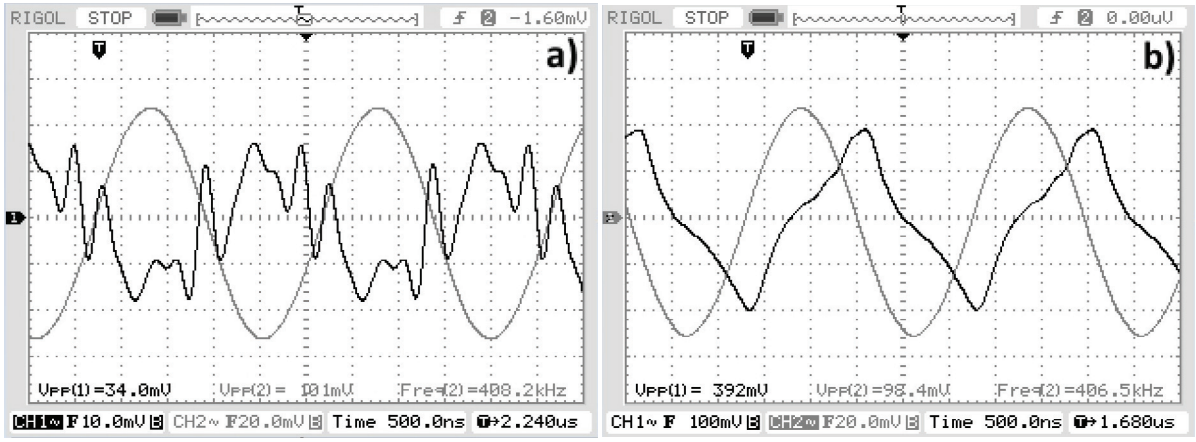

Figure 8. Oscilloscope captures of (a) the zero voltage level (CH1) achieved by the empty gradiometer and (b) the voltage acquired (CH1) when a sample is placed at the center of L_u. In both plots the gray waveform (CH2) corresponds to the sensed current crossing L_w.

observed, indicating a significant loss of information about M. This diminution can mask the magnetic saturation effects of the signals, where the samples do not have a linear response with H. Hence, all the successive measurements obtained with the oscilloscope were filtered using this criterion of f_c.

With respect to phase θ of the total impedance Z predicted in the computed data of figures 2(a)–(c), this is an intrinsic characteristic of our RL gradiometer system which is manifested as a delayed time between the current I crossing L_w with respect to the induced voltage V on L_u (empty). This delay can be represented as a phase-shift $\Delta\theta$. In figures 6(a) and (b), measurements of I and V using $f = 100$ kHz and 400 kHz, respectively, are shown. V is directly measured with the oscilloscope and I is determined by the Hall effect. In these plots, 2.38 μs and 0.52 μs are the respective absolute time delays. The same procedure is followed to perform the phase calibration sweeping the frequency of I, then each measured delay is transformed into gradian units and the dependence of $\Delta\theta$

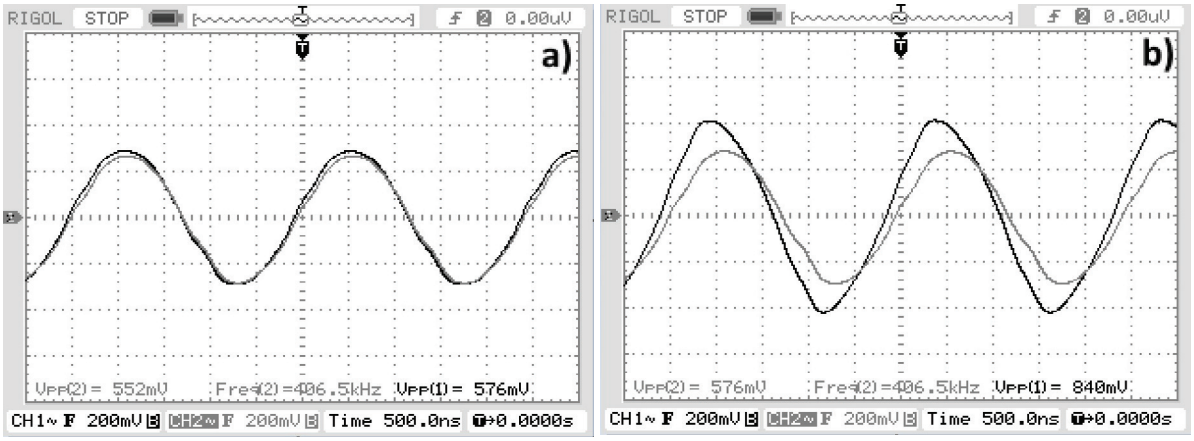

Figure 9. Oscilloscope registers of the differential voltages ΔV_{u-r} (CH1) and ΔV_{d-r} (CH2) (a) without sample near L_u, and (b) with the ferrofluid sample near L_u.

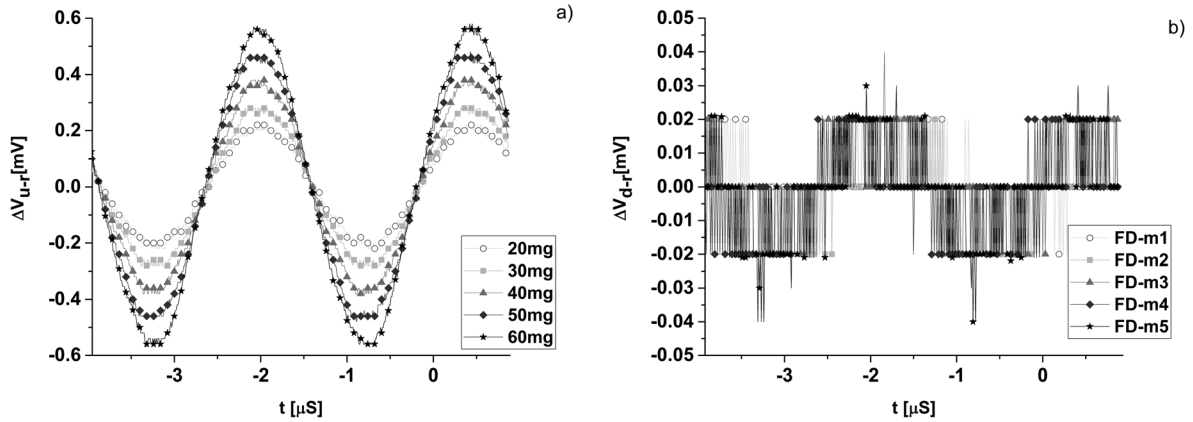

Figure 10. Registers of the differential voltages of (a) ΔV_{u-r} and (b) ΔV_{d-r}, for samples FD-m1, FD-m2, FD-m3, FD-m4 and FD-m5 placed within the center of L_u.

versus f is plotted in figure 7(a). In this plot, an increase in $\Delta\theta$ along f is observed according to figure 2(b) and the experimental data are fitted by linear regression (data not shown) with approximately 0.04° per kHz of absolute slope and 1.2° of intercept. In the same way, in figure 7(c) $\Delta\theta$ has been mathematically compensated by I and V waveforms corresponding to $f = 100$ kHz and 400 kHz, reaching a clear collapse between I and V at both frequencies. On the other hand, according to the specifications of the Hall probe used, this sensor has a constant 80 ns of signal delay, which remains implicit within the already subtracted $\Delta\theta$. Thus, this phase-shift compensation procedure to the empty gradiometer signals permits us to differentiate any other phase modification, which must be due to the sample introduced in the sensing system. Indeed, with this compensation a better reconstruction of the DHL can be guaranteed, avoiding the inclusion of undesired artifacts in the estimated magnetization waveform.

4. Results and discussion

4.1. Measuring the s/n ratio

In order to evaluate the *s/n* ratio of our gradiometer system connected with R_s, a second experiment using $f = 406.5$ kHz was conducted. When there was no sample in the gradiometer, $V_{\text{pp-g}} = 34$ mV was the peak to peak amplitude of the signal recorded in CH1 of figure 8(a); this is called our zero-voltage level. In contrast, $V_{\text{pp-s}} = 392$ mV was measured when sample FF1 was introduced (see figure 8(b)). Even though the estimated *s/n* ratio is 21.2 dB, $V_{\text{pp-s}}$ depends on the weight, shape and composition of the sample, and $V_{\text{pp-g}}$ also depends on the geometric characteristics of the gradiometer. With fast observation of the minor signal plotted in figure 8(a), the influence of the applied field of 406.5 kHz with superimposed high-frequency noise is still evident. This effect indicates that the electrical properties of L_u and L_d are not identical. Even this noise can be attenuated by reducing the digital cut-off frequency, but it could be detrimental for a accurate determination of M, so we decided for subsequent experiments to subtract the corresponding $V_{\text{pp-g}}$ from all the measurements (this is different for each f).

4.2. Determining the correction factor k

Further measurements with FF1 now in Stage 3 (using the reference coil L_r) were performed to verify the validity of the ideal of point charge behavior, implying that M only induces magnetic flux on the upper coil L_u. In figure 9(a), the differential

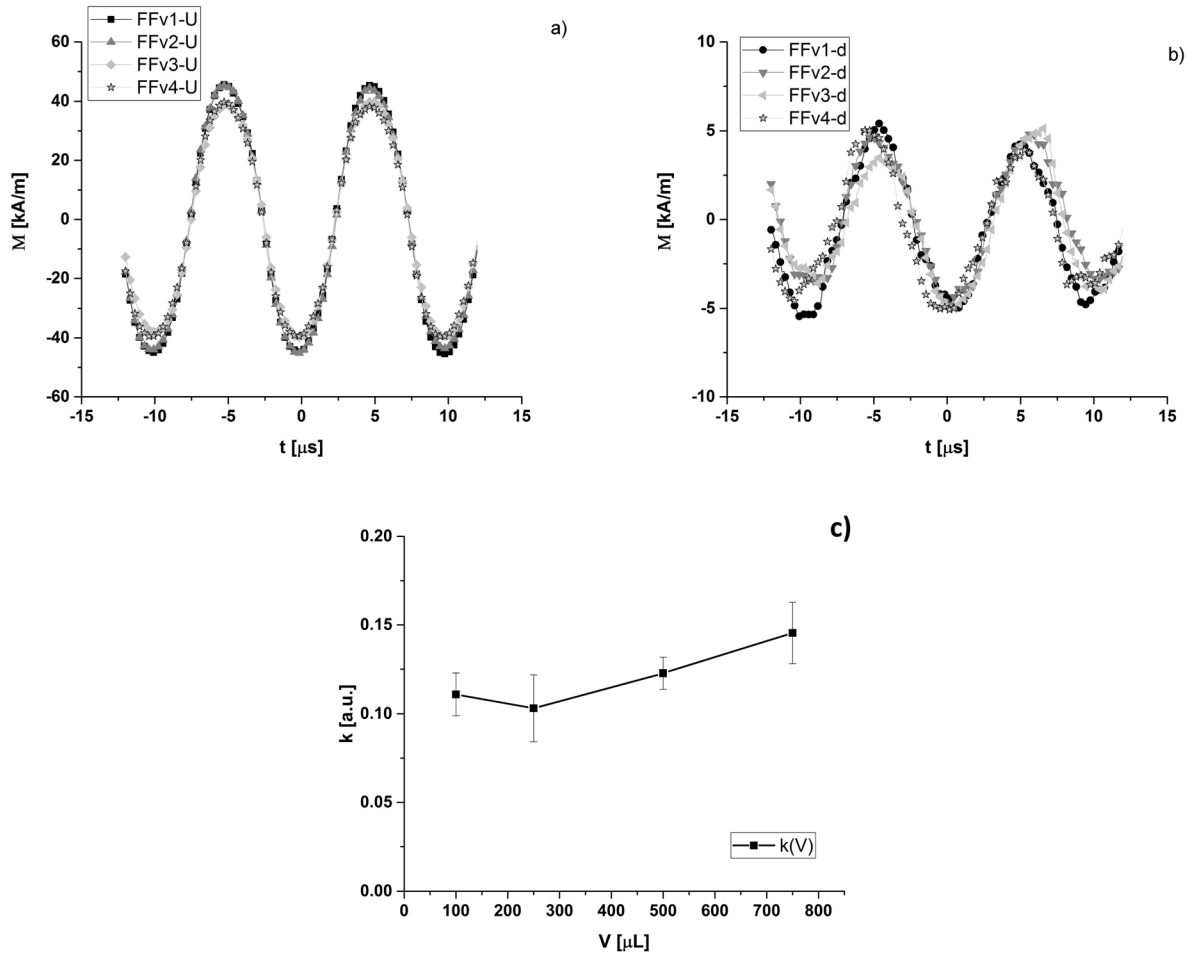

Figure 11. Computed registers of the differential voltages of (a) ΔV_{u-r} and (b) ΔV_{d-r}, for FF-v1, FF-v2, FF-v3 and FF-v4, showing the fraction of M seen by the array once the sample is placed within the center of L_u. (c) Correction parameter k as a function of the total sample volume V.

voltages ΔV_{u-r} (CH1) and ΔV_{d-r} (CH2) are obtained without any sample near to L_u. Indeed, small discrepancies between their amplitudes are found, reaching $\Delta V_{u-r} - \Delta V_{d-r} = 24$ mV, which is very similar to the zero-level amplitude. Later, the sample was approximated to L_u; the corresponding measurements of ΔV_{u-r} and ΔV_{d-r} are displayed in figure 9(b). In this trial, both signal amplitudes increased compared with the empty case. Thus, the sample influences both coils of the gradiometer exhibiting a non-ideal magnetized charge, and a factor correction k becomes necessary.

The last experiment was repeated but with the ferrofluid sample replaced by the flat plane samples FD-m1, FD-m2, FD-m3, FD-m4 and FD-m5. In figures 10(a) and (b) the respective measurements of ΔV_{u-r} and ΔV_{d-r} are displayed. Through rapid observation of both kinds of waveforms it can be concluded the amplitude of ΔV_{u-r} increases along with the mass increment, while the amplitude of ΔV_{d-r} remains around zero. Hence, the behavior of flat samples is like that of ideal point charges (i.e. $k \approx 0$) and stands in contrast to that of the ferrofluid samples.

In general, the ferrofluid samples have a volumetric presentation V which can include a determined concentration η of magnetic nanomaterial dispersed in water. Therefore, dependence between k, V and η can be expected. So, similar experiments (like that in figure 9) were performed but using the ferrofluid samples FF-v1, FF-v2, FF-v3 and FF-v4, which have the same mass of MNPs but dispersed in different volumes of water. For each sample, the respective waveforms ΔV_{u-r} and ΔV_{d-r} were used to compute the fraction of M seen by each differential array and the estimations are shown in figures 11(a) and (b). As is expected, a dependence on the sample volume is observed, evidencing a clear non-point-like behavior; indeed the dependence of k along V is displayed in figure 11(c).

4.3. Determination of the DHL and computing the SAR of the ferrofluid

The DHLs of the identical samples FF1, FF2 and FF3 are now constructed. Once the gradiometer has been properly placed into L_w and zero-level voltage reached the samples were placed inside L_u. Their average factor $k = 0.14 \pm 0.01$ was obtained by configuring Stage 3 of the *RL* sensors and applying equation (9) to the recorded ΔV_{u-r} and ΔV_{d-r} signals. Returning to Stage 2, the induced signals on the gradiometer due to M, including the magnetic field waveform, were stored for offline

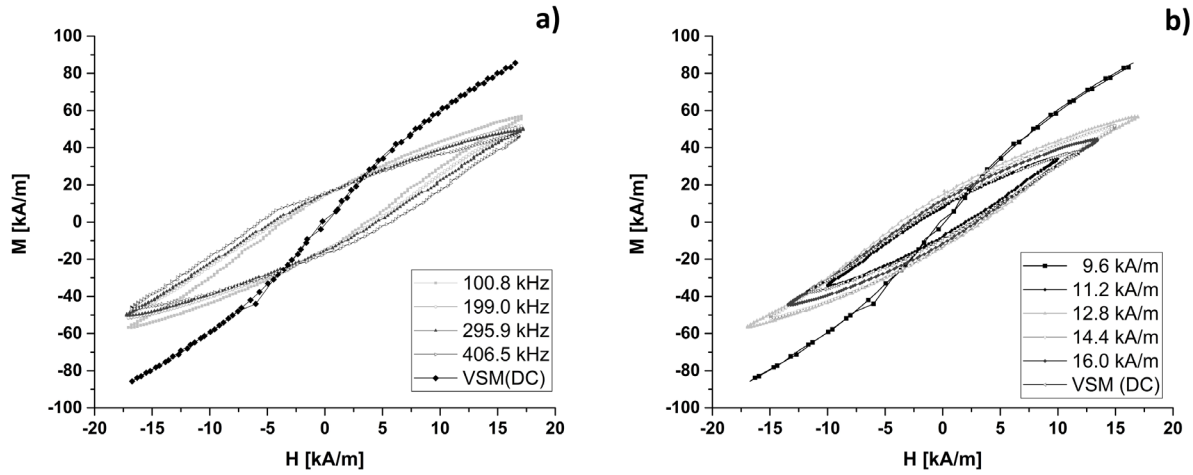

Figure 12. DHL reconstruction of F1 setting (a) $H = 16.0$ kA m^{-1}, 100.8 kHz $< f <$ 406.5 kHz and (b) $f = 100.8$ kHz, 9.6 kA m^{-1} $< H <$ 16.0 kA m^{-1}.

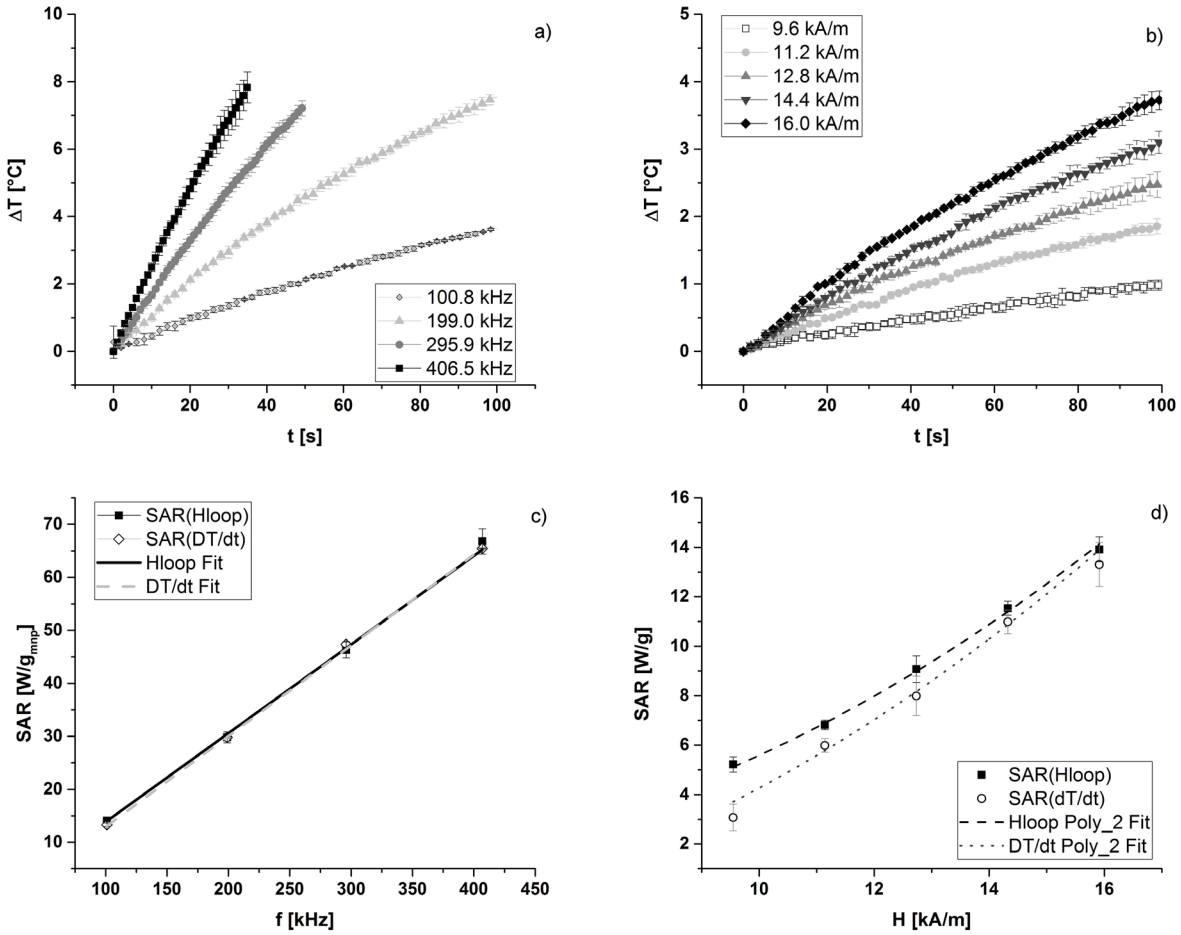

Figure 13. Averaged temperature rise of FF1, FF2 and FF3 (a) using 16.0 kA m^{-1} and f variable and (b) using $f = 100.8$ kHz and H variable. Also, the estimated SAR values using (c) H constant and (d) f constant, respectively. The dashed and solid lines correspond to linear and quadratic data regressions.

analysis. Subsequently, the next steps were followed to build the DHL:

- The zero-level was subtracted from the gradiometer measurements.
- Phase-shift compensation was carried out over the subtracted signals for each applied frequency.
- M was computed by solving equation (8) and numerically integrating the last compensated signal.
- A plot H versus M was made.

In figure 12(a), four typical overlapped DHLs are shown. These loops correspond to sample FF1, setting $H = 16.0$ kA m^{-1} while the frequency swept the interval

100.8 kHz $< f <$ 406.5 kHz. The DC hysteresis loops measured with the PPMS Versalab is also shown (dark dots), depicting a superparamagnetic-like behavior. As is expected, their inner areas increase with the applied f as a lagged hysteresis loop.

In other successive measurements, more DHLs are reconstructed setting $f = 100.8$ kHz and sweeping the amplitude interval 9.6 kA m^{-1} $< H <$ 16.0 kA m^{-1}. Figure 12(b) displays five typical overlapped loops, also corresponding to FF1. There, the characteristic concentric DHL evolves from an almost linear response (ellipsoid shape), which is gradually deformed when H increases due to a magnetic saturation trend.

Additionally, the internal areas of the DHL were computed through the Polygon Area function of the Origin platform, obtaining the values for the dissipated power loss P, which are used to compute the characteristic SAR of FF1, FF2 and FF3 in units of W g^{-1}. Finally, in order to compare these estimations of SAR, the parameters H and f are established and the traditional calorimetric procedure followed for the three ferrofluids. Figures 13(a) and (b) show the average temperature increments along time of FF1, FF2 and FF3. The error bars represent the standard deviation. While the intensity H is fixed in the measurements in figure 13(a), the parameter f remains constant in figure 13(b). In all those plots, the temperature slopes in the time interval 8 s $< t <$ 20 s were estimated using linear regression and equation (2) with $C_p = 4.175$ J g^{-1} K^{-1}. Furthermore, in figure 13(c) two dependences of SAR versus f are displayed: the dark squares correspond to the DHL procedure and gray circles are measurements with the calorimeter device. The respective estimated SAR rates are 0.171 and 0.167 W g^{-1} kHz^{-1}, having discrepancies of 2%. Moreover, 0.056 and 0.063 W g^{-1} per kA m^{-1} [2] are the corresponding coefficients of the quadratic regression computed for the measured dependence of SAR versus H^2 displayed in figure 13(d), having a discrepancy of 11%. Therefore this set of measurements suggests that our procedure for determining DHL is reliable.

5. Conclusions

A new dynamic hysteresis meter was designed taking into account several important details related to the construction of M. In contrast to similar published works, a quite detailed procedure for obtaining the magnetization of the samples was conducted. Due to the incorporation of resistive loads into the gradiometer system, its Q factor was modified, permitting a significant attenuation of the high-frequency noise induced on the coil sensors. Also, the phase-shift compensation and the digital filtering of the signals were analyzed, establishing a criterion for validation of the low-pass cut-off frequency. This avoids information loss for M and also the inclusion of artifacts on the resultant signals. Furthermore, a third coil was used as a reference sensor; this allowed an estimation of the correction factor k for the obtained waveforms due to the non-point-like behavior of the ferrofluid samples. Thus, the parameter k of point-like discs and volumetric ferrofluid samples was satisfactorily studied. Finally, the DHL of three ferrofluid samples was obtained with the new experimental setup considering sweeps of f and H separately. The computed estimates of SAR show good agreement with the corresponding measurements obtained following the traditional calorimetric method.

Acknowledgments

The authors wish to thank the Mexican institution CONACYT for the scholarship of the undergraduate and graduate students. Thanks also to Thomas M. Trent and Kurt Alejandro Kanzler for reviewing the language of the paper.

ORCID iDs

A H Sámano https://orcid.org/0000-0003-2684-313X
J C Estrada https://orcid.org/0000-0002-6727-3500
M E Cano https://orcid.org/0000-0002-3334-0082

References

[1] Bekovic M and Hamler A 2010 Determination of the heating effect of magnetic fluid in alternating magnetic field *IEEE Trans. Magn.* **46** 552–5
[2] Nakamura K, Ueda K, Tomitaka A, Yamada T and Takemura Y 2013 Self-heating temperature and AC hysteresis of magnetic iron oxide nanoparticles and their dependence on secondary particle size *IEEE Trans. Magn.* **49** 240–3
[3] Connord V, Mehdaoui B, Tan R P, Carrey J and Respaud M 2014 An air-cooled Litz wire coil for measuring the high frequency hysteresis loops of magnetic samples-A useful setup for magnetic hyperthermia applications *Rev. Sci. Instrum.* **85** 093904
[4] Guibert C, Fresnais J, Peyre V and Dupuis V 2017 Magnetic fluid hyperthermia probed by both calorimetric and dynamic hysteresis measurements *J. Magn. Magn. Mater.* **421** 384–92
[5] Garaio E, Collantes J M, Plazaola F, Garcia J A and Castellanos-Rubio I 2014 A multifrequency eletromagnetic applicator with an integrated AC magnetometer for magnetic hyperthermia experiments *Meas. Sci. Technol.* **25** 115702
[6] Garaio E, Collantes J M, Garcia J A, Plazaola F, Mornet S, Couillaud F and Sandre O 2014 A wide-frequency range AC magnetometer to measure the specific absorption rate in nanoparticles for magnetic hyperthermia *J. Magn. Magn. Mater.* **368** 432–37
[7] Garaio E, Sandre O, Collantes J-M, Garcia J A, Mornet S and Plazaola F 2015 Specific absorption rate dependence on temperature in magnetic field hyperthermia measured by dynamic hysteresis losses (ac magnetometry) *Nanotechnology* **26** 015704
[8] Mazon E E *et al* 2017 A high-resolution frequency variable experimental setup for studying ferrofluids used in magnetic hyperthermia *Rev. Sci. Instrum.* **88** 084705
[9] Mazon E E, Sámano A H, Calleja H, Quintero L H, Paz J A and Cano M E 2017 A frequency tuner for resonant inverters suitable for magnetic hyperthermia applications *Meas. Sci.Technol.* **28** 095901
[10] Armitage D W, LeVeen H H and Pethig R 1983 Radiofrequency-induced hyperthermia: computer

simulation of specific absorption rate distributions using realistic anatomical models *Phys. Med. Biol.* **28** 31

[11] Szasz O, Szigeti G and Szasz A 2016 Connections between the specific absorption rate and the local temperature *Open J. Biophys.* **6** 53–74

[12] Palihawadana-Arachchige M, Nemala H, Naik V M and Naik R 2017 Effect of magnetic dipolar interactions on temperature dependent magnetic hyperthermia in ferrofluids *J. Appl. Phys.* **121** 023901

[13] Hadadian Y, Azimbagirad M, Navas E A and Pavan T Z 2019 A versatile induction heating system for magnetic hyperthermia studies under different experimental conditions *Rev. Sci. Instrum.* **90** 074701

[14] Rosensweig R E 2002 Heating magnetic fluid with alternating magnetic field *J. Magn. Magn. Mater.* **252** 370

[15] Carrey J, Mehdaoui B and Respaud M 2011 Simple models for dynamic hysteresis loop calculations of magnetic single-domain nanoparticles: application to magnetic hyperthermia optimization *J. Appl. Phys.* **109** 083921

[16] Veryaskin A V 2018 *Magnetic gradiometry in Gravity, Magnetic and Electromagnetic Gradiometry* (CA: Morgan & Claypool Publishers) pp 2–19

[17] Zilstra H 1967 *Experimental Methods of Magnetism* ed E P Wohlfarth (http://dl.icdst.org/pdfs/files3/243f5e29b41236646ffe756552ef5e5f.pdf)

[18] Ota S, Yamada T and Takemura Y 2015 Dipole-dipole interaction and its concentration dependence of magnetic fluid evaluated by alternating current hysteresis measurement *J. Appl. Phys.* **117** 17D713

[19] Ueda H and Watanabe T 1975 Several problems about sensitivity and frequency response of an induction magnetometer *Geophysics* **22** 107–28 (https://tohoku.repo.nii.ac.jp/?action=pages_view_main&active_action=repository_view_main_item_detail&item_id=11186&item_no=1&page_id=33&block_id=38)

[20] Petcharoen K and Sirivat A 2012 Synthesis and characterization of magnetite nanoparticles via the chemical co-precipitation method *Mater. Sci. Eng.* B **177** 421–7